Neutron and x-ray scattering study of phonon dispersion and diffuse scattering in (Na,Bi)TiO_3-$x$$BaTiO_3$ single crystals near the morphotropic phase boundary

Chengtao Luo*
Materials Science and Engineering, Virginia Tech, Blacksburg, Virginia 24061, USA

Dipanshu Bansal
Materials Science & Technology Division, Oak Ridge National Laboratory, Oak Ridge, Tennessee 37831, USA

Jiefang Li and Dwight Viehland
Materials Science and Engineering, Virginia Tech, Blacksburg, Virginia 24061, USA

Barry Winn
Quantum Condensed Matter Division, Oak Ridge National Laboratory, Oak Ridge, Tennessee 37831, USA

Yang Ren
X-ray Science Division, Argonne National Laboratory, Argonne, Illinois 60439, USA

Xiaobing Li and Haosu Luo
Shanghai Institute of Ceramics, Chinese Academy of Sciences, 215 Chengbei Road, Jiading, Shanghai 201800, China

Olivier Delaire†
Mechanical Engineering and Materials Science Department, Duke University, Durham, North Carolina 27708, USA and Materials Science & Technology Division, Oak Ridge National Laboratory, Oak Ridge, Tennessee 37831, USA

(Received 2 May 2017; revised manuscript received 25 September 2017; published 10 November 2017)

Neutron and x-ray scattering measurements were performed on $(Na_{1/2}Bi_{1/2})TiO_3$-x at%$BaTiO_3$ (NBT-xBT) single crystals ($x = 4$, 5, 6.5, and 7.5) across the morphotropic phase boundary (MPB), as a function of both composition and temperature, and probing both structural and dynamical aspects. In addition to the known diffuse scattering pattern near the Γ points, our measurements revealed new, faint superlattice peaks, as well as an extensive diffuse scattering network, revealing a short-range ordering of polar nanoregions (PNR) with a static stacking morphology. In samples with compositions closest to the MPB, our inelastic neutron scattering investigations of the phonon dynamics showed two unusual features in the acoustic phonon branches, between the superlattice points, and between the superlattice points and Γ points, respectively. These critical elements are not present in the other compositions away from the MPB, which suggests that these features may be related to the tilt modes coupling behavior near the MPB.

DOI: 10.1103/PhysRevB.96.174108

I. INTRODUCTION

It has been nearly 50 years since the first atomic-level ferroelectric microscopic theory was published by Cochran and Anderson [1], which was based on their study of lattice dynamics. The concept of soft-modes in the phonon dispersions was introduced to describe the slowing of vibrational frequency, all the way to freezing, for transverse optical phonon modes (TO) during ferroelectric transformations. The TO mode condensation results in static ionic displacements below the transition temperature, thereby producing large permanent spontaneous polarizations and crystal lattice distortions. The soft-mode concept describes the common characteristics many proper and improper ferroelectric transformations, most known polar transformations, including antiferroelectric ones, although some are thought to arise from a change in magnetic order or electronic/orbital structure. The soft-mode theory has been experimentally validated by inelastic neutron scattering (INS) and Raman spectroscopy measurements in a number of compounds, most notably in conventional ferroelectric systems such as $PbTiO_3$ [2,3]. The physical picture of the ferroelectric transition in disordered, so-called relaxor systems, remains less clear, however. X-ray diffuse scattering and INS are powerful experimental techniques for investigating the specific microstructure and mechanisms underpinning piezoelectric behavior through phonon analysis. Here, we apply these experimental techniques to the study of NBT-xBT.

Based on the unique characteristics of "relaxor" ferroelectrics—and in particular the ultrahigh piezoelectric properties of $Pb(Mg_{1/3}Nb_{2/3})O_3$-$PbTiO_3$ (PMN-PT) and $Pb(Zn_{1/3}Nb_{2/3})O_3$-$PbTiO_3$ (PZN-PT)—significant efforts have been directed at extending the soft-mode theory in order to account for their unusually slow dynamical transition and relaxation mechanism [4–7]. Relaxor systems have also been developed in Pb-free perovskite solid solutions, which exhibit many of the properties of Pb-based systems [8]. Following the

*lchentao@vt.edu
†olivier.delaire@duke.edu

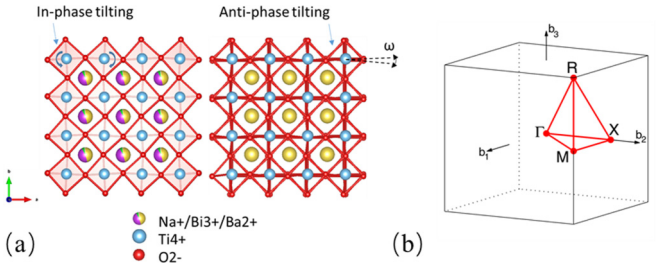

FIG. 1. Background figures: (a) NBT-BT superlattice structure comparison ($P4bm$ for NBT-7BT and R3c for NBT); (b) high-symmetry point notation in reciprocal space for pseudocubic NBT-BT.

strategy of adding $PbTiO_3$ (PT) to PMN to produce remarkably high piezoelectric response in the PMN-PT solid solution, $(Na_{1/2}Bi_{1/2})TiO_3$ (NBT) alloyed with $BaTiO_3$ (BT) was also found to form an analogous solid solution between relaxor and normal ferroelectrics, with a morphotropic phase boundary (MPB) between rhombohedral (R) and tetragonal (T) phases [8]. Consequently, $(Na_{1/2}Bi_{1/2})TiO_3-x$ at%$BaTiO_3$ (NBT-xBT) and $(Na_{1/2}Bi_{1/2})TiO_3-x$ at%$(K_{1/2}Bi_{1/2})TiO_3$ (NBT-xKBT) ceramics and single crystals have been developed and studied [9,10].

In addition to two different kinds of intrinsic ferroelectric polarization, NBT-xBT also features two improper ferroelectric oxygen octahedral tilt systems in R and T phases, which can be identified by characteristic superlattice structures ($P4bm$/$R3c$), as shown in Fig. 1(a). In the Glazer notation, these octahedral tilt systems are designated as in-phase $a^0a^0c^+$ and anti-phase $a^-a^-a^-$ [11]. These different tilt systems result in distinct superlattice Bragg reflections in reciprocal space, which are readily identified in diffraction experiments. The in-phase tilt belongs to T phase ($P4bm$) and has superlattice peaks at the M point, while the anti-phase one belongs to R phase ($R3c$) and has superlattice peaks at the R point. M and R points have crystallographic indices of the form ½(ooe) and ½(ooo), respectively (o for odd and e for even). The locations of both the M and R points in reciprocal space are illustrated in Fig. 1(b) in the case of a pseudocubic lattice [12]. These rotational modes are the result of acoustic phonon modes that condense at the Brillouin zone boundaries. Although these are typically nonpolar modes, they have been reported to couple with polarization through rotostriction [13]. To explain the phase coexistence and the relaxor behavior, a model of polar nanoregions (PNRs) similar to that developed for Pb-based relaxors was also introduced [4,14]. In details, the coexistence of M-point derived ($P4bm$) PNRs and R-point derived (R3c) PNRs has already be used to explain electron diffraction result [10,14]. Yao *et al.* reported the volume fraction of the M-point derived ($P4bm$) PNR increases with increasing x as the MPB is approached [14]. The PNR concept is a popular model to link the extraordinary properties of Pb-based ferroelectric relaxors [15–18] to the microstructure. Presently, one of the main problems in applying PNR-based models in NBT-xBT system is that the coupling of the two oxygen tilt systems is still unclear and requires further investigations.

The analysis of the atomic displacements in these tilt systems can be performed via x-ray diffraction (XRD) [19,20], electron microscopy [21,22], or neutron scattering techniques [4,23], which enable one to track the phase transition and domain structures. Neutron scattering in particular has been widely used to study different types of relaxors including the Pb-free ones [4,23–25]. For NBT-xBT solid solutions, different geometric patterns in the diffuse (elastic) scattering were previously investigated to characterize the different phases [23]. Further, INS studies were performed on the undoped system NBT [26,27]. Here, we extend these prior studies and investigate trends in mode softening, superlattice points, and diffuse scattering in more detail in the NBT-xBT system, in order to probe the dynamic mechanism underlying piezoelectric/relaxor behavior. Extensive characterization near the MPB of the NBT-xBT system was performed by means of synchrotron single-crystal XRD and INS experiments. In addition to the known diffuse scattering patterns near the Γ points, a superlattice point and a diffuse scattering network was observed, revealing a short-range ordering in the PNR static stacking morphology. In our studies of atomic dynamics with INS, two acoustic-like modes are identified, with a possible connection to the diffuse signal seen in XRD. One is between the superlattice points, and the other is between the superlattice points and Γ points. These features are not seen in compositions away from the MPB, which may shed light on specific dynamics near the MPB that impact the high piezoelectric response.

II. EXPERIMENT

High-quality single crystals of NBT-xBT ($x = 4\%$, 5%, 6.5%, and 7.5%) were grown by a top-seeded solution growth method. The compositions of the solid solutions in the as-grown condition were determined by inductively coupled plasma atomic emission spectrometry (ICPAES).

Neutron scattering measurements were performed using the hybrid spectrometer (HYSPEC [28,29], BL-14B) at the spallation neutron source (SNS) at Oak Ridge National Lab (ORNL). Using HYSPEC, the dynamical structure factor S(Q, E) was mapped for crystals of NBT-5BT (mass: 1.984 g) and NBT-6.5BT (0.882 g) at room temperature and 600 K. Additional compositions NBT-4BT (11.457 g)/NBT-5BT (39.009 g)/NBT-7.5BT (14.814 g) were measured at 300 K/540 K/700 K.

High-energy XRD measurements were performed on beam line 11-ID-C ($\lambda = 0.11725$ Å and $E = 105.8$ keV) at the Advanced Photon Source (APS) at Argonne National Laboratory (ANL). The 2D images were collected in the forward direction using a Perkin-Elmer large area detector. The diffraction patterns were analyzed using the FIT2D software. The distance from sample to detector and instrumental parameters were determined by refining the profiles from standard CeO_2 samples.

III. RESULTS

In this study, all the reciprocal space results were indexed under a pseudocubic lattice. The first neutron dataset is based on the (H K 0) planes to focus on the M points while the second neutron dataset is based on the (H H L) planes to focus on the R points. The energy integration range of all the elastic mappings is from −1 to 1 meV. The energy ranges of INS results are 0

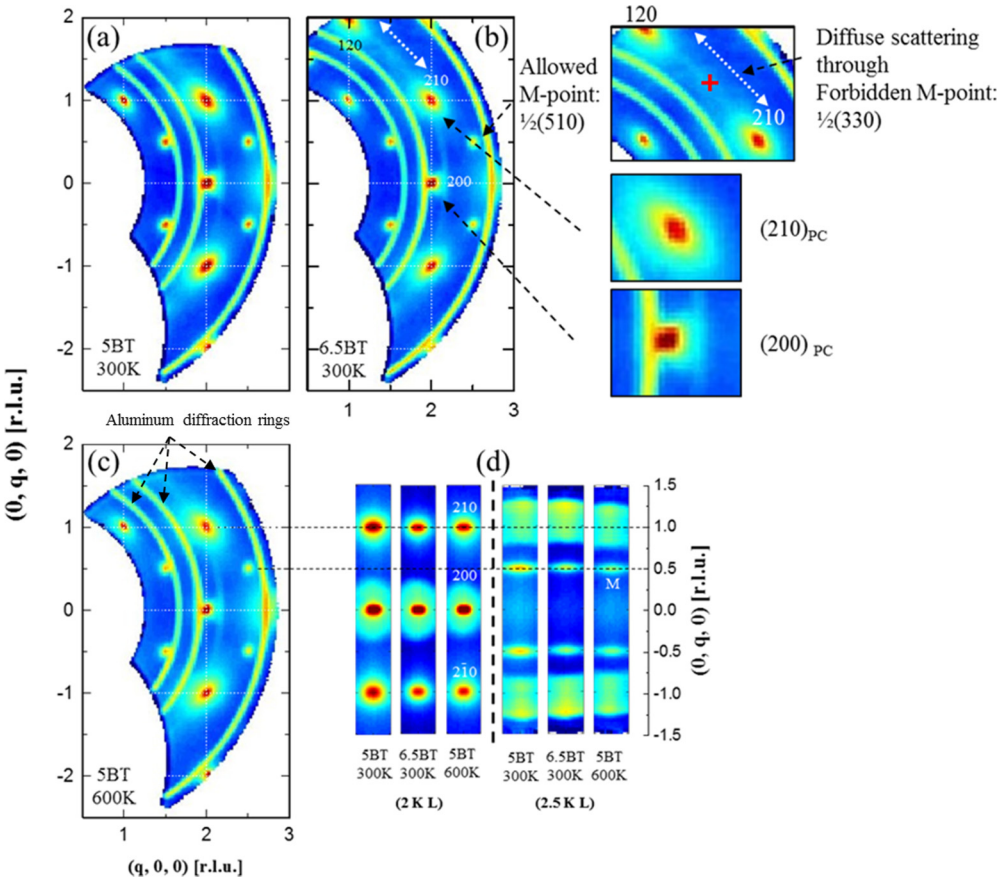

FIG. 2. Elastic neutron scattering patterns of (a) NBT-5BT at 300 K, (b) NBT-6.5BT at 300 K, (c) NBT-5BT at 600 K in the (H K 0) plane and (d) (2KL)/(2.5KL) plane. The horizontal and vertical axes are along [H00] and [0K0] directions, respectively, in the (H K 0) plane, and [0 0 L] and [0 K 0] directions for the (2KL) and (2.5KL) plane, respectively.

to 13 meV for first dataset, and 0 meV to 20 meV for second one. Both INS datasets were supplemented by corresponding XRD results.

All the INS results use the symmetry labels convention of Cowley *et al.* (Appendix I of Ref. [30]) to refer to the different normal modes. All the color maps represent the neutron scattering intensity plotted on a logarithmic scale, which is unformed in each sample.

The temperature points selected in this work are based on the characteristic temperatures of NBT-5.6BT [31]. In particular, the depolarization temperature T_d is 403 K, dielectric maximum temperature (Curie temperature) T_m is 560 K, and Burns temperature T_B is near 650 K.

A. Elastic neutron scattering in (H K 0) plane

The elastic neutron scattering patterns in Figs. 2(a)–2(c) focused on the (H K 0) planes of NBT-5BT at 300 K (a), NBT-6.5BT at 300 K (b), and NBT-5BT at 600 K (c). The slices were centered on the (200) zone and contained multiple M points. Due to the fact that the $^1/_2(3 \pm 1\ 0)$ points overlapped with an Al powder diffraction ring from the sample holder, the M-point data discussed later will only consider the $^1/_2(5 \pm 1\ 0)$ reflections.

In general, changes in temperature and composition did not appear to significantly impact the resulting elastic neutron scattering patterns shown for these slices. Similar diffuse scattering near (200) and (210) were already observed in prior XRD [31] and neutron [23] studies. In both compositions investigated herein, the scans showed oval-shaped scattering patterns around (210) with a ⟨110⟩ orientation and half-X-shaped scattering around (200), as showin in right panels in Fig. 2(b). These features are characteristic of the tetragonal side of the MPB [4,23]. Generally, the diffuse scattering for NBT-5BT was more intense than in NBT-6.5BT. Note that NBT-5BT is closer to the MPB, and features enhanced piezoelectric properties.

In-phase oxygen octahedral tilting superlattice reflections at M points, were evident in all slices. These M points were surrounded by isotropic diffuse scattering intensity in the (H K 0) plane. In the top-right panel of Fig. 2(b), one can note the presence of diffuse scattering intensity connecting the (1 2 0) and (2 1 0) zones, which crosses the forbidden point ½(3 3 0), as shown by the dashed white line with arrows and red cross. Here, the dashed white line with arrows is parallel to the actual diffuse scattering and used only to indicate the directions. This type of diffuse scattering connection was not observed toward the M-point ½(510), as will be further discussed with respect to INS studies.

We observed both symmetry-allowed [½(5 1 0), ½(3 1 0)] and symmetry-forbidden [½(3 3 0)] superlattice reflections in the tetragonal phase of NBT-xBT with the $P4bm$ space group

symmetry. The forbidden M point $\frac{1}{2}(h\ h\ l)/(-h\ h\ l)$ is due to the unique oxygen octahedron connection [see Fig. 1(a)]. In the (H K0) plane and for the case of $P4bm$, neighboring oxygen octahedra have opposite tilting directions, which generates the superlattice structure $a^0a^0c^+$; this finding also indicates that the oxygen octahedra along $[H\ H\ 0]/[-H\ H\ 0]$ direction share a common tilting direction. Therefore the related superlattice points at $\frac{1}{2}(h\ h\ 0)/(-h\ h\ 0)$ are forbidden. And for single crystals, the further $\frac{1}{2}(h\ h\ l)/(-h\ h\ l)$ are also forbidden. Although this feature is not common in selected area electron diffraction (SAED) [14,32], it has been observed in results generated by high-energy XRD and software simulation based on the $P4bm$ symmetry [33,34]. In further discussions, we refer to the two types of M points as "allowed" and "forbidden." Both types of M points are shown in Fig. 2(b). The forbidden ½(3 3 0) is marked by a red cross.

In order to further compare the elastic scattering between the Bragg peaks and the M points, additional slices [Fig. 2(d)] along different directions were extracted from the same $S(Q, E)$ dataset. The slices on the left part of Fig. 2(d) illustrate the (2KL) planes covering the Bragg peak $(2\ 0\ 0)/(2 \pm 1\ 0)$, and those on the right-side show the (2.5KL) plane covering the M point $\frac{1}{2}(5 \pm 1\ 0)$. Note that the data in Fig. 2(d) shares the vertical [0 K 0] axes with Fig. 2(c), where dashed lines are drawn to help align the same Bragg peaks and M points. On the horizontal [0 0 L] axes of Fig. 2(d), the Q range covers a range of -0.2 and 0.2 reciprocal lattice units (r.l.u.). The scattering patterns in the planes (2KL) and (2.5KL) are clearly different from each other. The scattering near the Bragg peaks is isotropic, whereas the scattering near the M points shows a spindle-shaped feature along the [0 0 1] direction.

We now discuss the single-crystal XRD data measured with the APS beamline 11-ID-C. Figures 3(a)–3(f) illustrates the diffuse scattering pattern observed in the (H K 0) reciprocal plane. These data reveal diffuse ridges along the ⟨110⟩ directions, X-shaped patterns around (H 0 0), and superlattice peaks at M points as illustrated in the zoomed-in area in Fig. 3(g). These diffuse scattering patterns thus show similar features as those noted from the neutron investigations provided in Fig. 2.

As shown in Fig. 3, a clear (110)-oriented diffuse scattering intensity can be seen for both ($x = 5$ and 7.5) crystals. Strong X-shaped diffuse scatting features around the (q 0 0)/(0 q 0) reflections in Fig. 3 confirm that the elastic diffuse scattering features in the neutron data taken near (200) were incomplete since they were partly obstructed by aluminum rings. Unlike NBT [23], neither NBT-5BT nor NBT-7.5BT exhibit sharp changes in their diffuse scattering patterns with increasing temperature. Although XRD measurements were performed over a temperature range from 300 to 950 K, Figs. 3(a)–3(f) only show three temperatures: 300, 550 (near the dielectric constant maximum), and 700 K.

The evolution with temperature of the intensity of ½(3 1 0) M points is shown in Figs. 3(h)–3(i). In a uniform integration area around the ½(310), the intensities with same 2θ are integrated and the resulting curves of integrated intensity-versus-2θ are plotted. Curves for different temperatures are offset vertically to facilitate comparison and fitted by Lorentzian functions. The common feature of these two datasets is that there is no peak intensity jumps near the Curie temperature (560 K) and depolarization temperature (403 K), and such

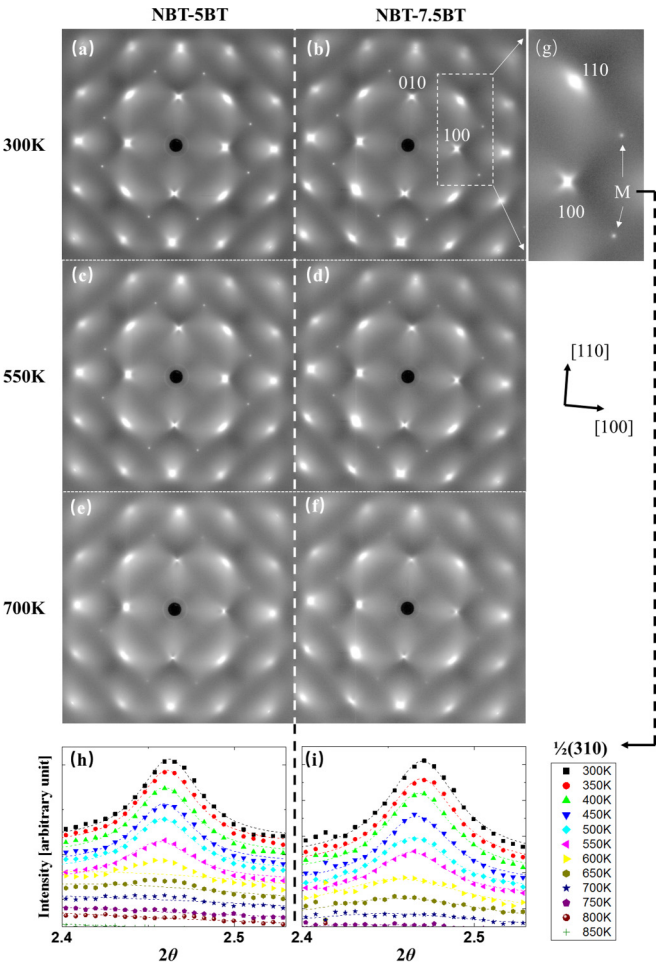

FIG. 3. XRD scattering patterns along the (H K 0) planes from [(a),(c), and (e)] NBT-5BT and [(b), (d), and (f)] NBT-7.5BT at [(a) and (b)] 300, [(c) and (d)] 550, and [(e) and (f)] 700 K. One area in (b) is enlarged in (g) to provide higher resolution pictures of the diffuse scattering features and M points $\frac{1}{2}(3 \pm 10)$. Integration of the intensity for ½(3 1 0) peak was made over a broad temperature range, as summarized in (h) NBT-5BT and (i) NBT-7.5BT. Fixed offsets were used between two neighboring curves to make comparisons easier.

intensity changing pattern will be compared to R point and discussed below. Furthermore, the FWHMs are not changed in both datasets under the 550 K. In details, FWHMs of NBT-5BT have a mean value of 0.0434 ± 0.0047 and a standard deviation of 0.0024, while FWHMs of NBT-7.5BT have a mean value of 0.0503 ± 0.0034 and a standard deviation of 0.0015. Such a temperature-independent FWHM of superlattice point is previously unreported. It indicates that the average size of M-point derived PNRs is also independent of temperature (within the resolution of our experiment). Also, the result indicates that M point ½(3 1 0) peaks are sharper in NBT-5BT than in NBT-7.5BT, showing such superlattice structure has a longer range ordering in NBT-5BT.

B. Inelastic neutron scattering in (H K 0) plane

The INS data around (200) Bragg peak is shown in Fig. 4, divided into two panels. The top row presents the data for

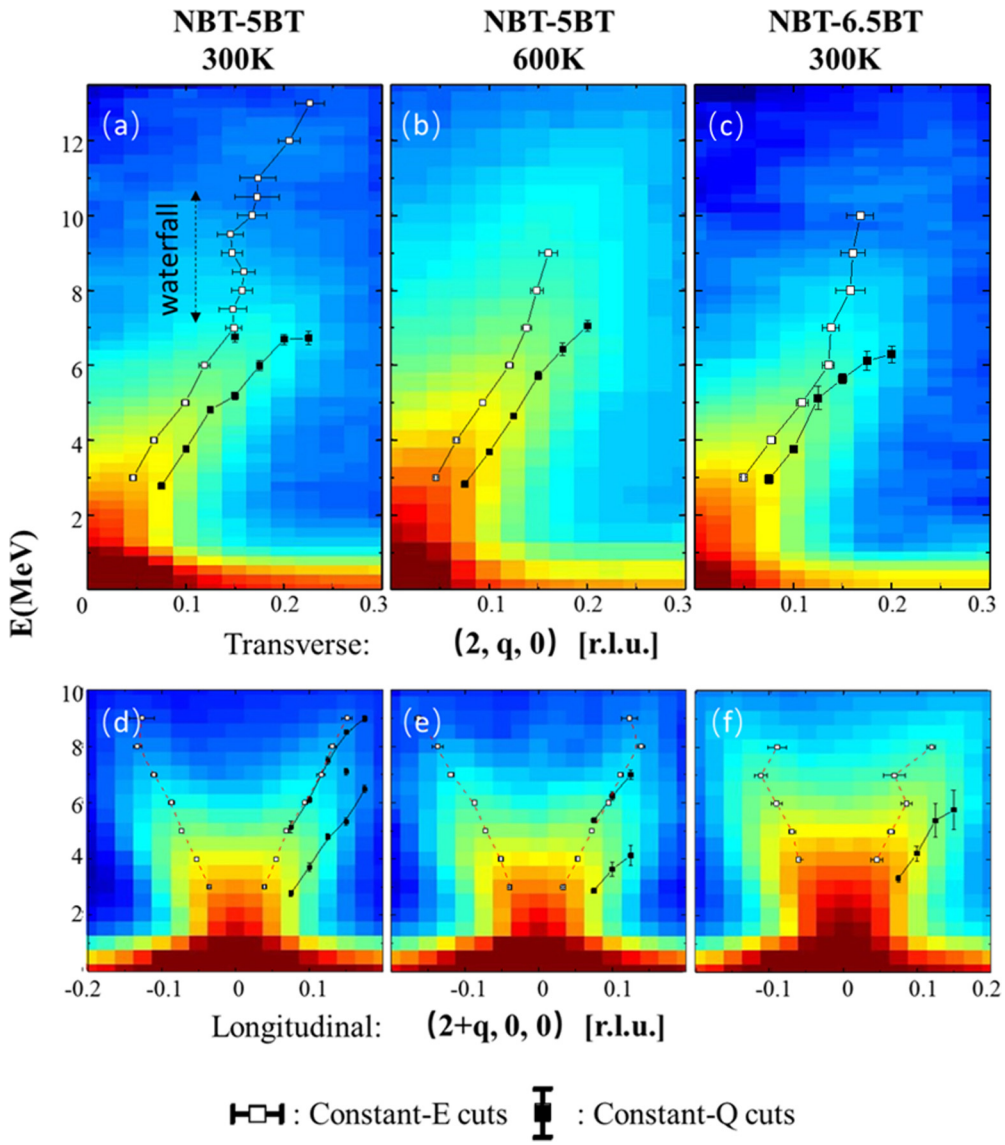

FIG. 4. Inelastic neutron scattering taken near the (2 0 0) Bragg peak. The figure is divided into three columns for [(a) and (d)] NBT-5BT at 300 K, [(b) and (e)] NBT-5BT at 600 K, and [(c) and (f)]NBT-6.5BT at 300 K. Likewise, it is divided into two rows for phonons in [(a), (b), and (c)] transverse modes and [(d), (e), and (f)] longitudinal modes.

transverse Δ_5 phonon modes, which were folded along the [H 0 0] axis. The data folding adds up the signals from (2, $-q$, 0) to (2, q, 0) to improve the statistical quality of the data for subsequent peak fitting. The folding is based on the pseudocubic symmetry, and is only used for transverse modes [Figs. 4(a)–4(c)]. The bottom row presents the data for the longitudinal Δ_1 phonon modes. Superimposed on these maps, the results of fits for the position of the peaks are shown, for fits performed using both constant-Q cuts and constant-E cuts. The constant-Q cut results are shown as black squares with vertical error bars, and results from constant-E cuts are indicated by the white squares with horizontal error bars.

In Fig. 4(a), the NBT-5BT crystal at 300 K exhibits a "waterfall" effect, where the TO phonon drops from 11 to 7 meV (into the TA mode) at the reduced phonon wave vector $q \sim 0.17$. This feature has been previously reported for both NBT [26] and PMN [35]. At 600 K [see Fig. 4(b)], the waterfall effect is less pronounced, which is indicated by the weaker TO phonon and its shifting along q. On the other side, the TA phonons are not obviously influenced by the temperature rising, and the TO mode still softened into the TA mode at the same q, showing the coupling of TA/TO modes is weakly dependent on temperature. In Fig. 4(c), the TO phonon of NBT-6.5BT can be seen to have a similar "drop" at the same $q \sim 0.17$; however, the extent of this drop is not as steep as that in Fig. 4(a). Compared to the different FWHM of NBT-5BT (0.0434) and NBT-6.5BT (0.0503) within Figs. 3(h)–3(i), the waterfall effect location here is not affected by the different composition, as well as the different sizes of the M-point derived PNR. Note that at 600 K, above the Curie temperature, the M points in the (HK0) plane are still observable, and here the persistence of the waterfall effect at this temperature indicates that the M-point PNR may play an important role in the lattice dynamics through the TO mode.

For the longitudinal Δ_1 phonon modes, the changes with temperature or composition are limited, as can be seen in

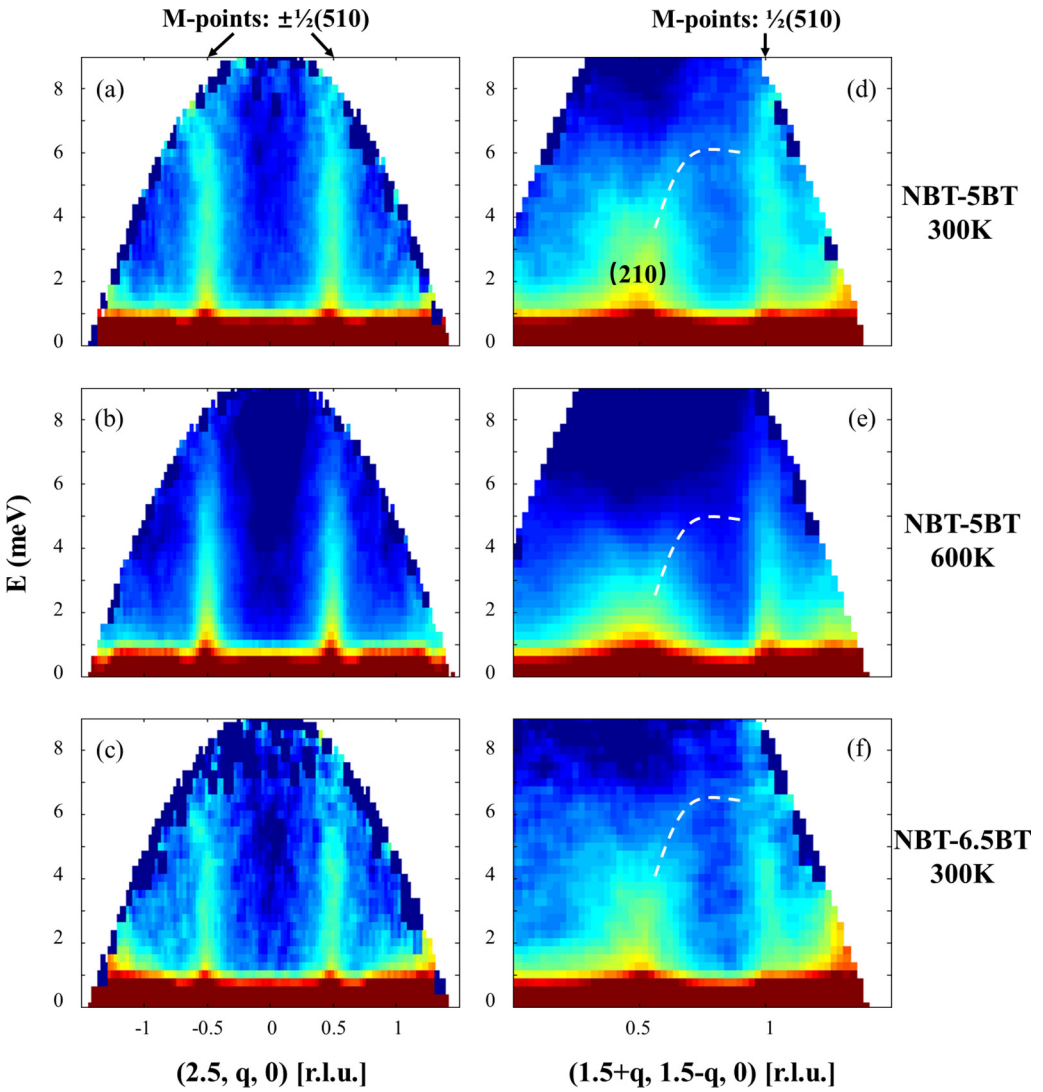

FIG. 5. Inelastic neutron scattering of [(a) and (d)] NBT-5BT at 300 K, [(b)and (e)] NBT-6.5BT at 300 K, and [(c) and (f)] NBT-5BT at 600 K. These data were taken along the [(a)–(c)] (2.5, q, 0) and [(d)–(f)] $(1.5 + q, 1.5 - q, 0)$. The energy columns near the allowed M points $\frac{1}{2}(5 \pm 10)$ are marked by arrows in (a) and (d).

Figs. 4(d)–4(f). Unlike previous studies involving NBT [26], the LO branches in Figs. 4(d)–4(f) are not observed to drop into the LA branches, nor was any LA branch splitting observed. We did, however, observe strong inelastic diffuse scattering near the in-phase superlattice reflections (M points), as shown in Fig. 5. Striking intense scattering "columns" (intensity signal spread over a broad range of energies at a fixed wave vector) were observed above the allowed M points up to about 8 meV, along the [2.5K0] direction [see Figs. 5(a)–5(c)]. These M-point columns showed no distinguishable q-broadening with increasing energy. The intensity and height of these columns were not significantly impacted by changes in temperature or BT content (5%/6.5%).

In addition to the intense columns at M points, intensity along [1 1 0] corresponding to transverse Σ_3 modes near the (210) zone is observed [see Figs. 5(d)–5(f)], connecting to an M-point column. In contrast, previous results in elastic scattering [Figs. 2(a)–2(c)] revealed that the allowed M points were not connected to any Bragg peaks by diffuse features in the (H K 0) planes. These Σ_3 modes in Figs. 5(d)–5(f) illustrate the similar connection to the M-point columns. Considering the compatibility relations between the Σ and M modes [30], the TA Σ_3 mode can only connect to the M_3 modes at the M points, and such TA Σ_3-M_3 connection is shown by the a dashed line in Figs. 5(d)–5(f). Thus the M-point columns can be identified as acoustic M_3 modes, which have the lowest frequency within all M modes and represents the oxygen octahedra in-phase tilting along c axis only.

C. Elastic neutron scattering in (H H L) plane

Figures 6(a)–6(f) show a panel of elastic neutron scattering patterns for NBT-7.5/5/4BT at temperatures of 300/540/700 K. These data were taken in the (H H L) plane. The horizontal and vertical axes are along the directions [0 0 L] and [H H 0], respectively.

First, multiple arc-shaped features can be seen for both NBT-5BT and NBT-7.5BT, which reflect varying sample mosaic quality. Second, both M and R points can clearly be seen to coexist. Detailed 1D cuts across different zones are shown

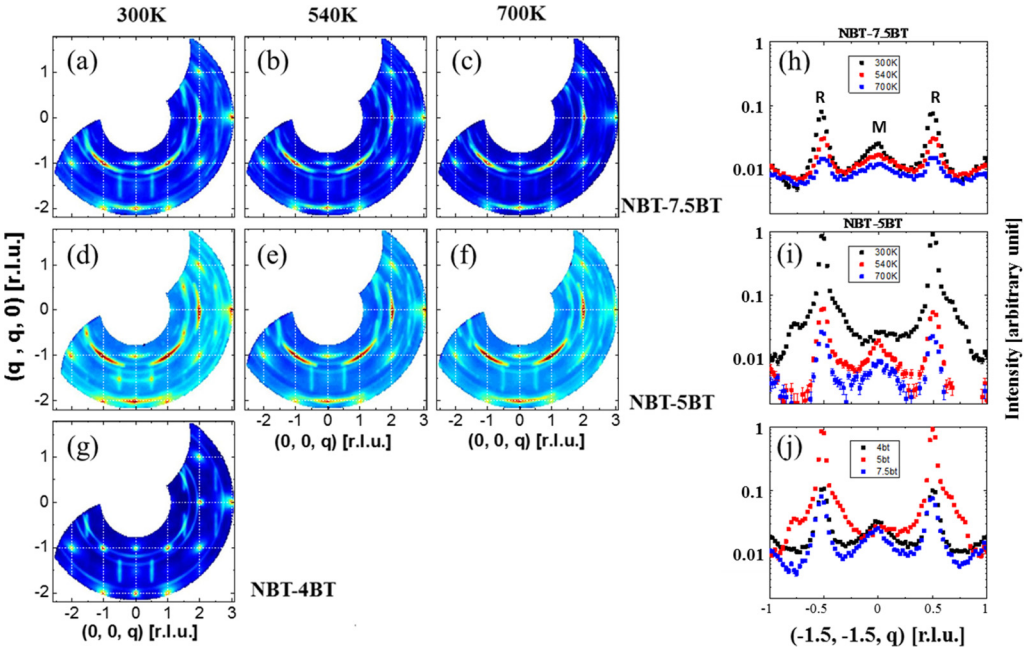

FIG. 6. (Left) [(a)–(g)] Neutron elastic scattering patterns taken in the (H H L) plane for (a)–(c) NBT-7.5BT, (d)–(f) NBT-5BT, and (g) NBT-4BT. The horizontal and vertical axes are along [0 0 L] and [H H 0], respectively. (Right) [(h)–(j)] Superlattice changes for NBT-xBT based in the (H H L) neutron data. Plots compare[(h) and (i)] the same BT contents at different temperatures, and in (j) the various BT contents at room temperature, respectively. The M point in (h)–(j) are from the forbidden ½(−3, −3, 0) zone.

in Figs. 6(h)–6(j). We note again that the M points ½(330) are forbidden in a perfect $P4bm$ space group, as indicated in reference to Fig. 2.

Figures 6(h)–6(j) focus on the [−1.5, −1.5, q] direction from the 1D cuts. These cuts cross both the forbidden M and the R points. In each sub-figure, the peaks from left to right are the R point ½(−3, −3, 1), the forbidden M point ½(−3, −3, 0) and the R point ½(−3, −3, −1), as indicated. One should note that the forbidden ½(−3, −3, 0) reflection has a weak, broad, and isotropic diffuse scattering shape. This is likely due to imperfections in the larger crystals. Here, the observations for the forbidden M points are quite different from the sharper and more intense behavior in the (H K 0) plane for the allowed M points. It is worth mentioning that the NBT-5BT crystal featured strong mosaic arcs at room temperature [black line in Fig. 6(i) and red line in Fig. 6(j)] near the R points, making the analysis of peak intensities [Figs. 6(h)–6(j)] difficult. So, the 1-D cut of NBT-5BT at room temperature will not be discussed. Compared to data shown in Fig. 3, the forbidden M-points in Figs. 6(h)–6(j) have similar features with changes in temperature between samples; specifically, the peak intensity decreases gradually with increasing temperature, but maintains the same FWHM.

An additional feature that can be noted in Fig. 6 is the unique vertical rod-shaped diffuse scattering around all the observable R-points along the [HH0] direction. Figure 7 proves that such rod-shaped scattering near the R-points arises from the projection of the X-shaped diffuse scattering within the measurement volume.

Figure 7 shows the 3D neutron elastic scattering patterns taken near the R point ½(−3, −3, 1). The 3D plots axes are along the [0 0 L], [H H 0], and [−H H 0] directions. The rod-shaped diffuse scattering becomes X-shaped in the 3D view. The diffuse streaks across the R-point are along the [1 0 0]/[0 1 0] directions [see Fig. 7(g)]. The isovalues of contour intensity at 300 K are set differently as 0.039 for NBT-7.5BT, 0.080 for NBT-5BT, and 0.037 for NBT-4BT. Also, the relative isovalues for 300 K/540 K/700 K of all samples are set as 8/6/5. These settings are decided in order to make the background signals in a similar level and show the 3D diffuse scattering shapes more clearly. Such X-shaped diffuse scattering near the R points is part of a much larger network, and here its boundaries are caused by the limited [−H H 0] range in $S(Q, E)$ dataset. With changes in temperature, these diffuse scattering streaks followed the R point in the center, and both were suppressed during heating process. Such intensity change pattern fits to the result from Figs. 6(h)–6(i).

These diffuse scattering streaks have two main characteristics. They exhibit [1 0 0]/[0 1 0] orientations, and they cross at the R-points. They are also observed in XRD measurements for NBT-5BT. Figure 8 shows the XRD scattering patterns obtained at APS for NBT-5BT at different temperatures. The scanning surface is tilted from the (H K 0) plane along the [0 1 0] axis in order to reach the near R points ½(5 1 1) and ½(5 3 1) in the enlarged regions. Smaller images on the right of Fig. 8(a) provide a magnified portion of the area focusing on the allowed M points at ½(5 0 1) and the R points at ½(5 1 1). Note also that Fig. 8(a) clearly shows the existence of the diffuse scattering network along [1 0 0]/[0 1 0] directions. The streaks shown in the magnified image to the right along the [0 1 0] direction crossed the allowed M points at ½(5 0 1) and the R points at ½(5 1 1). In addition, [1 0 0]-oriented streaks can also be seen on the left side of Fig. 8(a), as marked by dashed circles in multiple regions. These extra streaks across the superlattice point locations are also part of the diffuse scattering network.

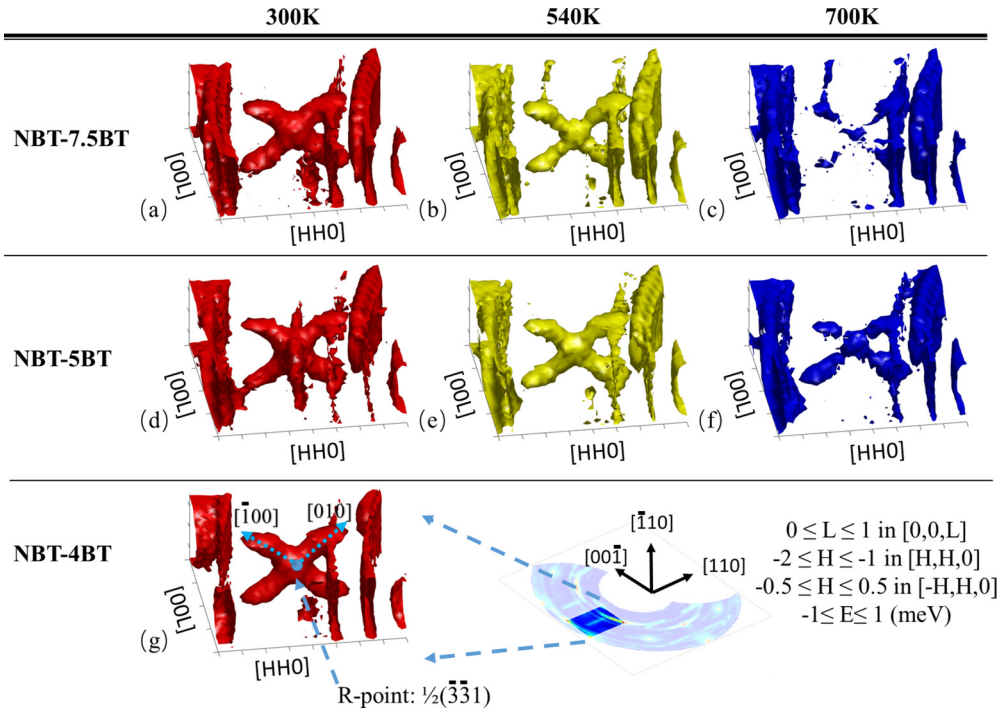

FIG. 7. 3D neutron elastic scattering patterns around the R point $(-3/2, -3/2, 0.5)$ for (a)–(c) NBT-7.5BT, (d)–(f) NBT-5BT, and (g) NBT-4BT. The three axes on each figure are along the [0 0 L], [H H 0], and [$-H$ H 0] directions. All the plots share the same range of [0, 1] in [0 0 L], $[-2, -1]$ in [H H 0] and $[-0.5, 0.5]$ in [$-H$ H 0]. Colors mark different temperatures, [(a), (d), and (g)] red at 300 K, [(b) and (e)] yellow at 540 K, and [(f) and (h)] blue at 700 K. Dashed arrows in (g) shows the selected 3D reciprocal space location based on Fig. 6(a). The isovalues of contour intensity at 300 K are set as (a) 0.039, (d) 0.080, (g) 0.037, and the relative isovalues for 300 K/540 K/700 K are 8/6/5.

The temperature dependence of the diffuse scattering network was also investigated. Figures 8(b) and 8(c) show the same mesh scans as Fig. 8(a) but at 550 and 700 K. At 550 K [Fig. 8(b)], the intensity along [1 0 0]/[0 1 0] decreased, the M-point intensity slightly decreased, and the R-point was suppressed. When heating to 700 K [Fig. 8(c)], both the diffuse scattering streaks and the M-point intensities strongly decreased to the point of vanishing.

The remaining synchrotron XRD data are summarized in Figs. 9(a) and 9(b), which focus on two different R points at ½(5 1 1) and ½(5 3 1) for various temperatures. The integration was accomplished in the same way as the M-point data process illustrated in Figs. 3(h)–3(i). Furthermore, Fig. 9(c) summarizes all the superlattice reflection fitting results with temperature for the various M and R points. All the peak fittings use Lorentzian functions. Red lines correspond to the same allowed M points at ½(3 1 0) as shown in Figs. 2 and 3. Blue and black lines pertain to the same NBT-5BT crystal, but show results from two different R points at ½(5 1 1) and ½(5 3 1). The peaks of ½(5 1 1) are too weak to be fit when temperature is higher than 400 K and the same for ½(5 3 1) peak at 450 K. The temperature difference of the intensity dropping between two R points is caused by the curvature of the detector sampling surface in reciprocal space, causing unequal deviations from the precise R-point locations. Thus the later discussion will only focused on ½(5 3 1).

Figure 9(c) illustrates an important difference between the integrated intensities associated with the allowed M and R points. The M points exhibit a nearly linear decrease in intensity with increasing temperature between 300 and 700 K. Moreover, no anomalies were found at any critical temperature. In contrast, the R points show a significant drop in intensity near the depolarization temperature T_d (403 K). Thus the data show that M and R points coexist only in the ferroelectric phase region—but at higher temperatures, only M points persist. Additionally, R-point ½(5 3 1) FWHMs of NBT-5BT have a mean value of 0.10042 ± 0.02454 and a standard deviation of 0.01323. Thus the R-point derived (R3c) PNR also has the same temperature-independent average size as M-point derived PNR.

D. Inelastic neutron scattering in (H H L) plane

This section examines the inelastic component of the neutron intensities in the (HHL) plane. Near the Bragg peak, Fig. 10 depicts transverse inelastic neutron scattering in the (002) zone. (Note that due to different propagation direction, the phonons are different from those discussed in Figs. 4 and 5.) Panels (a)–(g) illustrate the transverse phonon intensity and fitting results, with solid (open) dots indicating results from constant-Q (constant-E) cuts, respectively. It should be noted that the main part of fitting results, black and white dots, used the same fitting parameters of Fig. 4, while the red dots represent findings from thinner constant-Q cuts (integrated from smaller Q-range, from 0.04 to 0.02), compared to the black ones, and the triangular dots indicate results of fits with larger uncertainty. Despite these minor differences, there are two common points for all the panels in this figure: (a) the TO phonon dispersions reach their maximum at $E = 16$ meV when $q > 0.2$, and (b) the TA phonons were also nearly flat

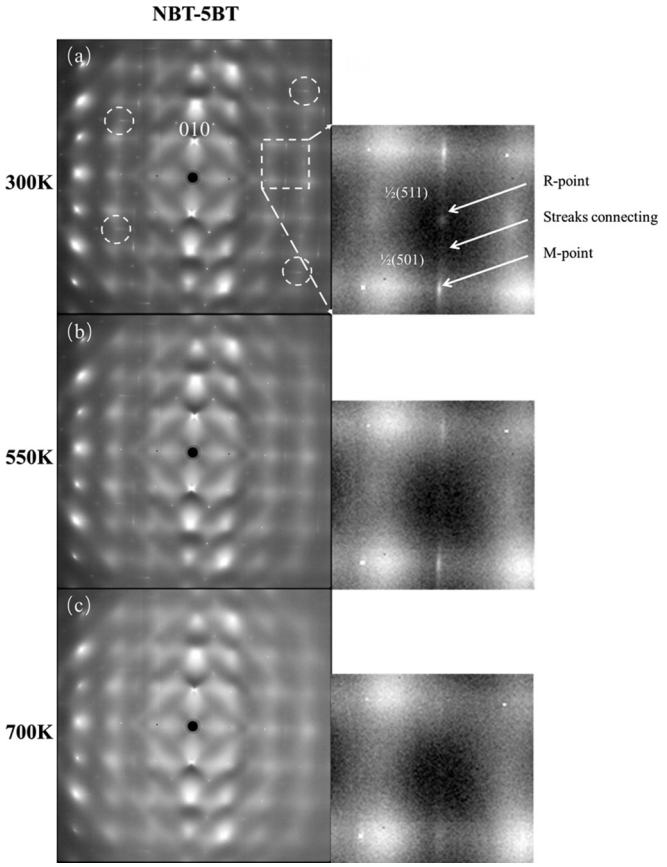

FIG. 8. XRD scattering patterns tilted from the (H K 0) planes for NBT-5BT at (a) 300, (b) 550, and (c) 700 K. The tilting angles were the same and were chosen by the maximum intensities of the R points at ½(5 1 1) and ½(5 3 1). The smaller images on the right of each panel are higher resolution area images in order to better show the allowed M points ½(5 0 1) and R points ½(5 1 1). Extra [1 0 0]-oriented diffuse scattering streaks are marked by dashed circles in (a).

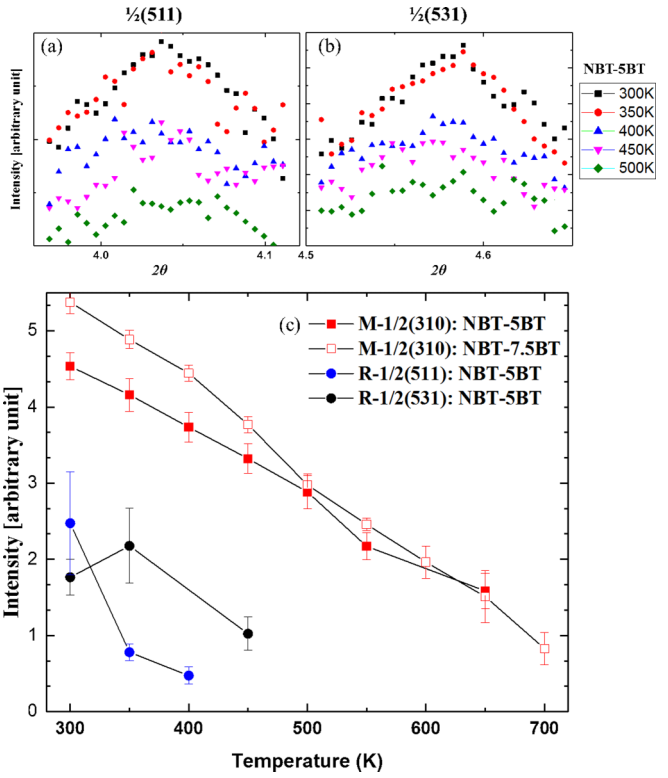

FIG. 9. (Top) [(a) and (b)] Integration of the NBT-5BT R-point intensity for (a) ½(511) and (b) ½(531) peaks with different temperatures. The integration process follows the Figs. 3(h)–3(i). There are fixed offsets between the two neighboring curves to make comparison easier. (Bottom) (c) Temperature-dependent superlattice point intensity changes of NBT-5BT and NBT-7.5BT for the allowed M point about ½(3 1 0) and R point about ½(5 1 1)/ ½(5 3 1). The peaks were all fit by Lorentzian functions.

in E for $q > 0.15$. Different from the Figs. 5(d)–5(f), the M point at the ½(110) is forbidden so there is no similar phonon connection here. Additionally, NBT-5BT and NBT-7.5BT have extra optical phonon signals near $q = 0$ and $E = 13$ meV at 300 K, which show softening at higher temperatures.

Similar to the bottom panel of Fig. 4, the longitudinal phonons showed little response to changes in temperature or composition. Figure 10(h) only shows the phonons from NBT-5BT at 300 K.

Finally, we discuss phonons near the forbidden M points. Figure 11 shows the INS intensity for transverse conditions near the M point $\frac{1}{2}(-3, -3, 0)$ in the (H H L) plane. The dataset was folded along the [H H 0] axis to improve statistics, so the R point is located in the middle, while the M point is situated on the right side.

Figure 11 also shows that, in addition to the elastic diffuse scattering streaks across the R and the M points, a broad inelastic "band" could be observed between these superlattice reflections. This signal could possibly correspond to damped fluctuations of soft tilt modes emerging from zone-boundary points. In contrast to the more clearly resolved acoustic phonons near the Bragg peaks (see Fig. 10), these inelastic bands showed a strong dependence on composition, being most intense for $x = 5\%$. The energy width of this feature is about 6–8 meV and changes little with temperature.

To confirm this feature, further slices (parallel to those in Fig. 11 along $[-H, H, 0]$) were made. We find the thickness of this band of intensity to be less than 0.2 r.l.u. along [HH0]. In addition, maps similar to those in Fig. 6 but integrating only over finite energy transfer were made. Without the Al-ring interference in the higher energy range, the shape of this band in the (H H L) plane shows negligible changes with energy until the cuts reach the $E > 8$ meV. Similar to the results in Figs 5(d)–5(f), from compatibility relations between the M and R modes [30], the symmetry character of this inelastic band could be related to M_3-Δ_2-R_{25}, which is also notated as T_2 mode in work of Swainson *et al.* [36]. The inelastic bands also help to explain the shape of the M-point energy columns (see Fig. 5) due to their same M_3 mode origin, as the intense scattering columns represent the perpendicular cuts of the bands at the M-point ends, and thus they have the same energy height (8 meV).

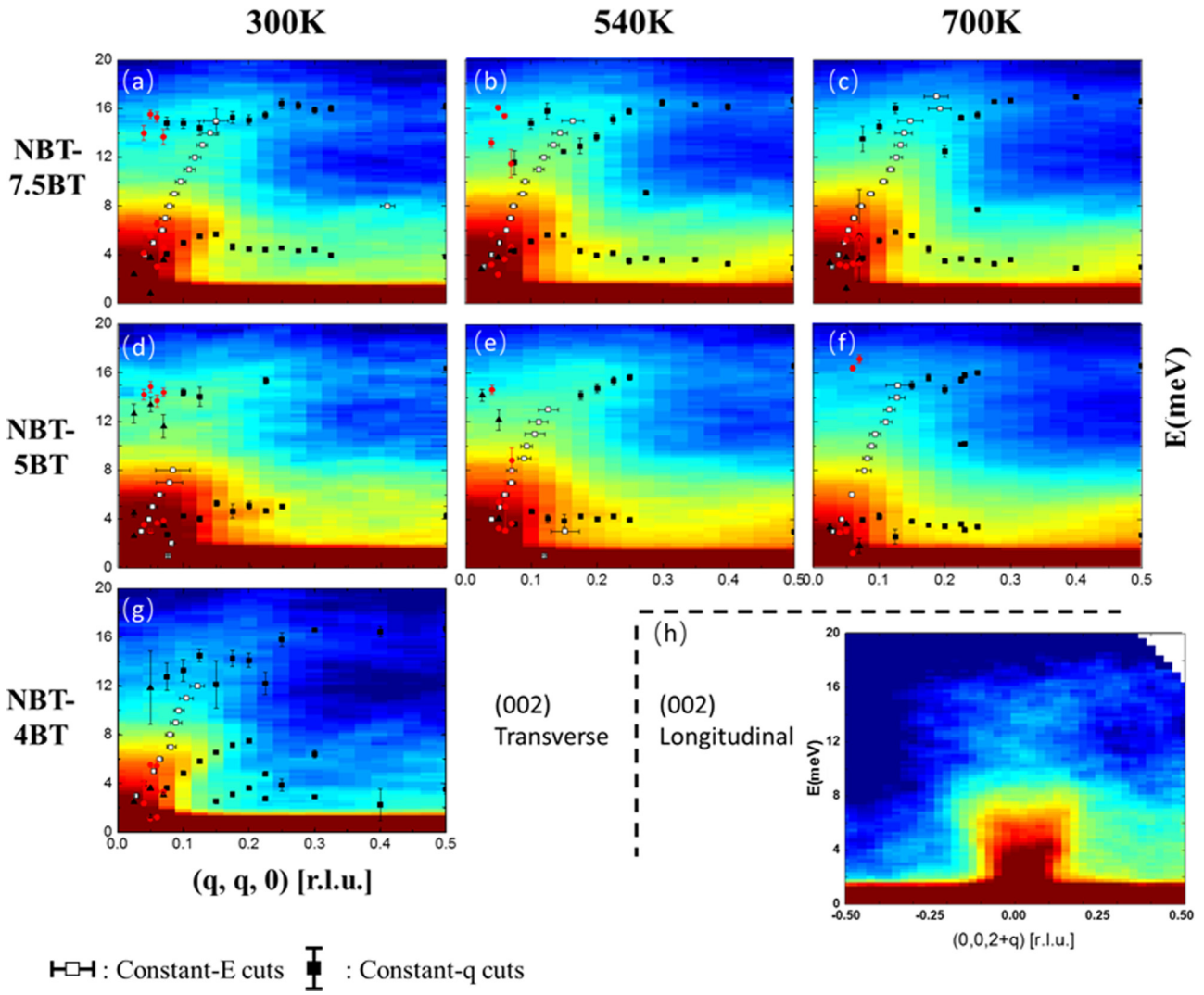

FIG. 10. Inelastic neutron scattering taken near the (0 0 2) zone in the (*H H L*) plane. The main image is divided into three rows for transverse acoustic phonons [(a)–(c)] NBT-7.5BT, [(d)–(f)] NBT-5BT, and (g) NBT-4BT, as well as three columns for [(a), (d), and (g)] 300, [(b) and (e)] 540, and [(c) and (f)] 700 K. Longitudinal phonons are shown in (h) NBT-5BT at 300 K. Solid dots indicating fitting results from constant-Q cuts, and open dots indicating those from constant-*E* cuts. The red dots represent fitting from thinner cuts in comparison to the black ones, and the triangular dots indicate fits with larger uncertainties.

IV. DISCUSSION

A. Model of diffuse scattering network

Before the discussion on model of diffuse scattering network which links superlattice points, a summary of observations in this work is list below.

Elastic. (1) Elastic diffuse scattering including oval-shaped and X-shaped diffuse scattering around different Bragg peaks are found in the (HK0) plane. Such a diffuse scattering pattern is characteristic of the tetragonal side of the MPB. (2) The ½(*H H* 0) *M* point is forbidden in both neutron and XRD elastic patterns, as previously reported [31]. However, our neutron results show weak and isotropic ½(−3, −3, 0) reflections in the (*H H L*) plane, while diffuse ridges cross the forbidden ½(3 3 0) in the (*H K* 0) plane. Additionally, these ridges become weak or absent towards the allowed *M* point ½(5 1 0). (3) Diffuse streaks are found in the elastic scattering channel in the vicinity of the R-points that are oriented along [1 0 0]/[0 1 0] (see Fig. 7). This feature is weakened significantly with increasing temperature near the dielectric constant maximum. These X-shaped features near the *R*-point superlattice reflections are previously unreported, and differ from those around the Bragg peaks. (4) The diffraction intensity (see Fig. 9) around the superlattice reflections reveals that the R-points experience an abrupt change near the ferroelectric phase transition at temperatures near T_d. In contrast, the intensity of the allowed *M* points gradually decreases with increasing temperature between 300 and 700 K. Also, our analysis of peaks at the *M* and *R* points shows nearly temperature-independent FWHM, which was not previously reported. Comparing the NBT-5BT and NBT-7.5BT, the integrated intensities at the *M* points are stronger at room temperature for NBT-7.5BT, while the peaks for NBT-5BT were sharper. (5) Diffuse streaks in the elastic scattering are observed between the *R* points and allowed *M* points along [1 0 0]/[0 1 0] (see Fig. 8). Such streaks have not been previously reported to our knowledge.

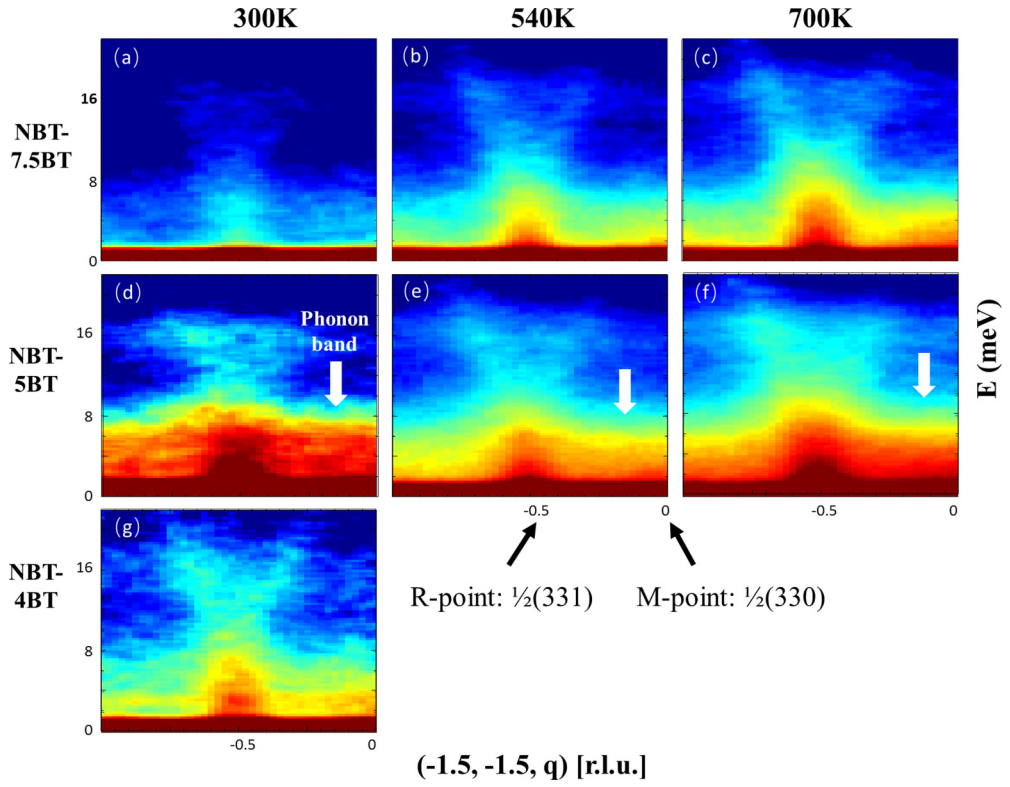

FIG. 11. Inelastic neutron scattering taken near the forbidden M point $\frac{1}{2}(-3, -3, 0)$ in the $(H\,H\,L)$ plane. The figure is divided into three rows for compositions of [(a)–(c)] NBT-7.5BT, [(d)–(f)] NBT-5BT, and (g) NBT-4BT, as well as three columns for temperatures of [(a), (d), and (g)] 300, [(b) and (e)] 540, and [(c) and (f)]700 K. All the images are plotted after being folded along $[H\,H\,0]$ axis.

Inelastic. (1) A waterfall effect is seen in the INS near the (200) Bragg peak (see Fig. 4). This waterfall feature has previously been reported in PMN and NBT relaxor-type solid solutions [26,35,37]. The waterfall feature is most pronounced near the MPB of NBT-5BT, which heretofore has not been reported. (2) Inelastic columns are observed near the allowed M points only (see Fig. 5), which are nearly temperature- and composition-independent over the ranges investigated for NBT-xBT. Similar broad columns have previously been reported for PMN by Swainson *et al.* [36], but were not been reported for NBT-xBT solutions. Near the (2 1 0) zone, the Σ_3-M_3 connection suggests that these results from in-phase tilting modes. (3) A broad "band" of inelastic scattering, about 8-meV wide, connecting R points and forbidden M points (see Fig. 11) is observed with INS. This band exhibited a strong intensity for the composition closest to the MPB. Note that the end of this band corresponds to the TA M_3 mode of the forbidden $\frac{1}{2}(3\,3\,0)$. We could not see similar intensity between the R points and allowed M point. This band and the inelastic columns (see Fig. 5) appear to have the same origin, with the columns representing the perpendicular cuts of the phonon band across the M points.

Figure 12 provides schematic summarizing observations. It incorporates both elastic [Fig. 12(a)] and inelastic scattering [Fig. 12(b)]. In Fig. 12(a), the white spheres represent the pseudocubic Γ points. The cyan sphere center is the R point. The blue spheres represent the forbidden M points shown in Fig. 6, and comparing the allowed M points in purple exhibited a spindle-shaped diffuse scattering [see Fig. 2(d)]. In addition to the superlattice reflections, strong elastic diffuse streaks are identified between them, comprising a filamentary network along [1 0 0]/[0 1 0] directions (see Figs. 7 and 8). The streaks network is illustrated in Fig. 12(a) by the red rods that connect the R points and allowed M points. Several rotations of the elastic diffuse scattering schematic model of Fig. 12(a) are provided in Fig. 12(c), which shows different 2D and 3D projections of the streaks network.

In Fig. 12(b), the phonons that cross the superlattice points are summarized and their locations are marked by double arrow symbols. The Σ_3-M_3 connections [see Figs. 5(d)–5(f)] are illustrated in Fig. 12(b) by red arrows. Also, the inelastic bands, M_3-Δ_2-R_{25} connections, between the forbidden M and R points (see Fig. 11) are shown as blue arrows in Fig. 12(b).

B. Diffuse scattering

Diffuse scattering ridges about the (1 00) zone along the (1 1 0) are well established in both PMN-PT and NBT-BT, as also reported herein. Such diffuse scattering ridges are a common feature to both Pb-based and Pb-free perovskite relaxor solid solutions. These ridges have been attributed to nanoscale inhomogeneous polarization distributions along a given direction [23]. In real space, they reflect the presence of polar nanoregions (PNR) that organize into hierarchical domain structures along (1 1 0). Another common point is that this type of diffuse scattering is suppressed in the high-temperature range ($>T_C$) for both Pb-based and Pb-free relaxors, which

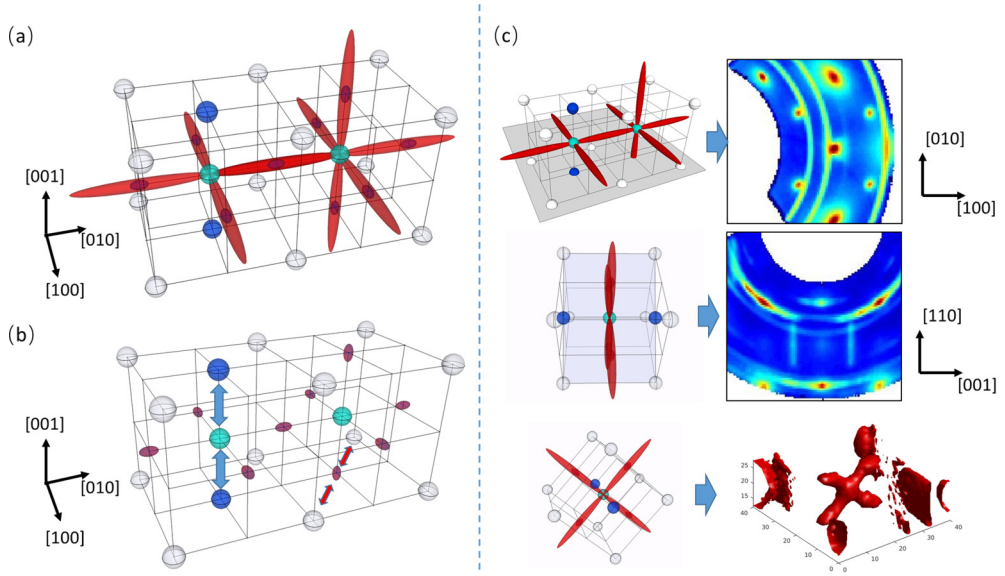

FIG. 12. Schematic of diffuse scattering streaks for NBT-xBT. (a) Elastic network across the superlattice points. (b) Inelastic phonon connections. (c) Demonstrations of how to offer the elastic slices from the schematic in (a). White spheres are Bragg peaks in the pseudocubic lattice, the R point is marked by cyan spheres, different types of M points are marked by blue spheres and purple spindle-shape spheres.

illustrates a correlation to the presence of polarization. However, it should be noted that for PMN-PT [38], the (1 1 0)-oriented diffuse scattering is significant in PMN on the rhombohedral side of the MPB while the diffuse scattering from PNRs is very weak or absent on the tetragonal side of the MPB in favor of a long-range, structurally ordered ground state.

NBT, on the rhombohedral side of the MPB, has been reported to exhibit "L" shape diffuse scattering patterns near (012) [23]; in contrast, NBT-5/7.5BT on the tetragonal side of the MPB features scattering patterns that are oval in shape and elongated in the ⟨110⟩ direction. Another study using neutron diffuse scattering by Ge *et al.* [4] investigated both A-site NBT and B-site PMN relaxors by comparing their similarities and differences in the geometry of the diffuse scattering patterns and the morphologies of the PNR distributions. The further diffuse scattering patterns of NBT and NBT-5.6BT showed A-site NBT-xBT has different PNR distribution, comparing to B-site PMN [4]. Specifically, prominent ridges in the elastic diffuse scattering intensity resulted in different types of contours. The ridges along the [1 0 0]/[0 1 0] directions cross at (h h 0)/(–h h 0) and generated "L" shaped patterns for NBT; conversely, the ridges along the [1 1 0] direction crossed at (h 0 0)/(0 k 0) and generated the X-shaped patterns for NBT-5/7.5BT. These ridges disappeared gradually upon heating above the cubic-to-tetragonal phase transition temperature of $T_{CT} = 523\,^{\circ}$C [4]. Thus these ridges across the Γ points can be used to characterize different types of PNRs. In this work, typical diffuse scattering patterns of NBT-xBT near the MPB are observed.

NBT-xBT differs from PMN-xPT in another notable aspect, by featuring improper ferroelectric oxygen octahedral tilt systems. Yao *et al.* [22,39] reported a hierarchical domain structure, where PNRs form on cooling within the geometrical restrictions imposed by the inheritance of a high temperatures ferroelastic phase consisting of nanometer-sized oxygen tilt domains. Dark-field imaging in TEM of the superlattice reflections revealed tilt domains of a few nanometers in size, which likely prevented a range of PNRs from achieving the elastic compatibility conditions of the relaxed state. Rather, a PNR distribution with a vortex morphology was recently shown to form [32]. Here, M and R points in the diffraction patterns are better characterizations of the coexistence phases/PNRs comparing to the diffuse scattering patterns near the Γ points [14]. The results of this study show that upon increasing temperature between 300 and 700 K, the intensity of the allowed M points gradually decreases, but the R-point intensity disappears near the ferroelectric phase transition (T_d). These findings lead to two conclusions: (a) the volume fraction of T-phase PNR changes linearly and is not significantly affected by the ferroelectric phase transition; (b) the changes of R-phase PNR is closely related to ferroelectric phase transition. Such PNR changing modes can successfully explain the origin of the frequency dispersion of temperature dependent of dielectric constant curves of NBT-xBT [40]. Near the T_d, there is T-phase/R-phase PNR coexistence, which causes the different frequency dispersion. Near the T_m, there is only T-phase PNR, so there is no dispersion at T_m. Further analysis reveals that the M- and R-point peaks have nearly temperature-independent FWHM. Thus it can be concluded that both T-phase and R-phase PNRs have nearly fixed average sizes. Comparing the NBT-5BT and NBT-7.5BT, it also can be concluded that stronger M points for NBT-7.5BT means T phase have more volume fractions herein, while the narrower FWHM for NBT-5BT signifies larger PNR average size as well as longer range of in-phase superlattice ordering.

As shown in the Fig. 12, the superlattice point linking diffuse scattering network shows a new feature of short-range ordering. The streak along [1 0 0]/[0 1 0] extends across the whole Brillouin zone between the R points and the allowed M points. This phenomenon not only reflects the M- and R-point coexistence, which is already used to explain the electron diffraction (TEM) result [10,14], but also indicates

these different types of tilt domains are stacking together along the [1 0 0]/[0 1 0] directions in short-range ordering. The long streaking along this direction may then demonstrate that the stacking sequence is not regular and that size of the tilt domains is not constant.

The net result of these competing processes is that the multiple domain ordering process (PNRs and tilt domains) may be prevented from reaching their elastically relaxed condition. If that is the case, then the polarization and different oxygen tilt systems would elastically constrain each other. Unlike in the PMN-xPT system, the PNR distribution would then not be as readily altered by applied field or stress (following adaptive phase theory), nor could the polarization of the monoclinic phase rotate as readily in an easy plane (following homogeneous theory). Rather the primary mechanism for shape change would be a length extensional mode, as recently shown by Ge *et al.* [19]. As a consequence, the piezoelectric properties of NBT-xBT may be significantly lower than the analogous properties reported for Pb-based relaxor single crystal systems. To enhance the piezoelectricity in these Pb-free system, going forward, one should consider how to decouple the polarization from the oxygen tilt system.

Differing with the allowed M points in (H K 0) planes, weak and isotropic diffuse scattering patterns are found near the forbidden ½(3 3 0) M points in (H H L) planes. These weak superlattice reflections are due to the imperfections associated with the translational invariance of the tetragonal phase with average $P4bm$ symmetry, and reflect the inherent inhomogeneity of the oxygen tilt and polarization subsystems. The stacking of the M-tilt and the R-tilt domains of nm-size, along with the presence of a high density of PNR boundaries, is far from the perfect symmetry for $P4bm$. Additionally, these forbidden M points are not interconnected to either the R points or allowed M points via elastic diffuse scattering. However, this only considers the static distortions determine from elastic diffuse scattering. In fact, one also needs to consider the phonon dynamics of the inelastic diffuse scattering in order to fully understand how the different modes are interconnected.

C. Inelastic neutron scattering

It is found that the lattice dynamics of NBT-xBT are similar to those previously reported for PMN [36], except for a few important details. The first is the presence of the waterfall effect, and the second is the presence of inelastic intensity columns near the allowed M points, which are very unusual given the fact that the line shape is localized in momentum, but broad in energy. No physical reason has yet been given to explain the existence of inelastic columns in PMN—and thus, by inference, with our report of their presence in NBT-xBT. Columns of inelastic intensity have been associated with a coupling of the lattice with other degrees of freedom [36]. Therefore it is reasonable to attribute them in NBT-xBT to the coupling between polarization and oxygen tilt through rotostriction [13] over limited length scales in an inhomogeneous relaxorlike system. This speculation is supported by the fact that the presence of these inelastic columns is clearly temperature-independent over the temperature range that we investigated (300–700 K). In prior research on PMN, the inelastic columns were found to soften with decreasing temperature below the dielectric maximum due to a softening of the optic phonon mode [36]. This behavior would suggest that the inelastic columns in NBT-xBT are not directly related to the formation of polarization, but rather persist into the high-temperature phase region where the M-type oxygen octahedral rotations remain present.

The close relationship between M-point columns and oxygen octahedral tilt systems is further confirmed from the presence of an acoustic mode connection that links allowed M points to Γ point [see Figs. 5(d)–5(f)]. This Σ_3-M_3 connection, which is not reported in NBT [26], correlates the M-point columns with TA M_3 modes. This acoustic Σ_3-M_3 mode is stronger near the MPB and notably temperature-dependent. The M_3 mode is related to the oxygen octahedral in-phase tiltings and thus could explain the temperature independence of the M-point columns. Comparing to the case of NBT [26], the M_3 mode is more intense and localized at M points in NBT-xBT near the MPB, presumably due to the enhanced M-point derived PNR with in-phase tiltings.

Another characteristic signature of the MPB region is the presence of inelastic bands connecting the R points to the forbidden M points in the (H H L) plane, as shown in Fig. 11. This band of intensity is following the M_3-Δ_2-R_{25} phonon branches. Similar to the Σ_3-M_3 connections, due to its low-energy and temperature independence at the M points, one can infer that this inelasitc band is the result of the coupling of the oxygen octahedral tilt modes. Indeed, this band-shaped M_3-Δ_2-R_{25} mode is distinctly different compared to the previous Σ_3-M_3 mode as well as the soft optic modes at the M-point columns of PMN [36]. The enhanced intensity of this inelastic band at the MPB indicates the existence of the intermediate Δ_2 mode, which helps coupling the M_3 and R_{25} tilting modes. The Δ_2 mode is also a tilting mode but related to the tilting along the [H H 0] axis. Similar to the bridging monoclinic phase in PZN-xPT at the MPB [41], such a mode could also lower the energy barrier between the M_3 and R_{25} tilting modes.

Thus, in addition to the importance of phase coexistence, a better understanding of dynamical features represents a key avenue for developing next-generation piezoelectric materials for potential applications. In other words, phase coexistence alone, which is a characteristic of many Pb-based and Pb-free compositions even away from MPB, cannot ensure high piezoelectric properties in Pb-free systems. Specific dynamical features, such as the inelastic bands or M_3-Δ_2-R_{25} mode are also required, to relax the constraints of the mixed oxygen tilt state. By redistributing energy between the different modes, the system can partially relax, and the oxygen tilt domains and PNRs can readjust and better accommodate each other. This process, in turn, can allow the material to express higher induced shape changes in response to stimuli in comparison to a response facilitated by a length extensional mechanism.

V. CONCLUSION

We systematically studied the NBT-xBT single crystals with neutron and x-ray scattering, for several temperatures and compositions across the MPB. Typical oval-shape [1 1 0] direction diffuse scattering patterns were observed near the Γ points (2 1 0), indicating the MPB compositions. In addition, a superlattice point linking diffuse scattering network was

observed, revealing a ferroelectric and short-range ordering PNR static stacking morphology. The evolution of superlattice points with temperature also showed that the size of related PNRs changes weakly with temperature. The lattice dynamics measurements focused on both phonon dispersions near the Γ points and superlattice points. A waterfall feature was observed in the TO mode near the (2 0 0) and was most enhanced in NBT-5BT at room temperature. For superlattice points, two types of dynamical signatures are found. One between the *M* and Γ points along the [1 1 0] direction, consistent with M-related tilting modes. The other between the *M* and *R* points along the [001] direction indicating the existence of an intermediate tilting mode, which could be essential in the high performance of those compositions near the MPB.

ACKNOWLEDGMENTS

Authors C.L. and D.V. would like to thank the ONRL-GO program for support of this work through the Laboratory Directed Research and Development Program of Oak Ridge National Laboratory, managed by UT-Battelle, LLC, for the U.S. DOE, and J.F.L. would like to thank the Office of Naval Research for the support of this work (N00014-13-1-0049). O.D. and D.B. acknowledge funding from the U.S. Department of Energy, Office of Science, Basic Energy Sciences, Materials Sciences and Engineering Division, under the Early Career Award No. DE-SC0016166. Authors X.L. and H.L. acknowledge the National Natural Science Foundation of China under Grants No. 51332009 and No. 61634007. The use of Oak Ridge National Laboratory's Spallation Neutron Source was sponsored by the Scientific User Facilities Division, Office of Basic Energy Sciences, US Department of Energy. This research used resources of the Advanced Photon Source, a U.S. Department of Energy (DOE) Office of Science User Facility operated for the DOE Office of Science by Argonne National Laboratory under Contract No. DE-AC02-06CH11357.

[1] W. Cochran, Dynamical, scattering and dielectric properties of ferroelectric crystals, Adv. Phys. **18**, 157 (1969).

[2] C. M. Foster, Z. Li, M. Grimsditch, S. Chan, and D. J. Lam, Anharmonicity of the lowest-frequency A1(TO) phonon in $PbTiO_3$, Phys. Rev. B **48**, 10160 (1993).

[3] I. Tomeno, J. A. Fernandez-Baca, K. J. Marty, K. Oka, and Y. Tsunoda, Simultaneous softening of acoustic and optical modes in cubic $PbTiO_3$, Phys. Rev. B **86**, 134306 (2012).

[4] W. Ge, C. P. Devreugd, D. Phelan, Q. Zhang, M. Ahart, J. Li, H. Luo, L. A. Boatner, D. Viehland, and P. M. Gehring, Lead-free and lead-based ABO_3 perovskite relaxors with mixed-valence A-site and B-site disorder: Comparative neutron scattering structural study of $(Na_{1/2}Bi_{1/2})TiO_3$ and $Pb(Mg_{1/3}Nb_{2/3})O_3$, Phys. Rev. B **88**, 174115 (2013).

[5] K. Hirota, Z. G. Ye, S. Wakimoto, P. M. Gehring, and G. Shirane, Neutron diffuse scattering from polar nanoregions in the relaxor $Pb(Mg_{1/3}Nb_{2/3})O_3$, Phys. Rev. B **65**, 104105 (2002).

[6] C. Stock, G. Y. Xu, P. M. Gehring, H. Luo, X. Zhao, H. Cao, J. F. Li, D. Viehland, and G. Shirane, Neutron and x-ray diffraction study of cubic [111] field-cooled $Pb(Mg_{1/3}Nb_{2/3})O_3$, Phys. Rev. B **76**, 064122 (2007).

[7] G. Y. Xu, Probing local polar structures in PZN-xPT and PMN-xPT relaxor ferroelectrics with neutron and x-ray scattering, in *International Conference on Frustration in Condensed Matter*, edited by H. A. Katori *et al.* (Iop Publishing Ltd, Bristol, 2011), p. 012081.

[8] S. O. Leontsev and R. E. Eitel, Progress in engineering high strain lead-free piezoelectric ceramics, Sci. Technol. Adv. Mater. **11**, 044302 (2010).

[9] T. Takenaka and H. Nagata, Current status and prospects of lead-free piezoelectric ceramics, J. Eur. Ceram. Soc. **25**, 2693 (2005).

[10] C. Ma, H. Guo, S. P. Beckman, and X. Tan, Creation and Destruction of Morphotropic Phase Boundaries through Electrical Poling: A Case Study of Lead-Free $(Bi_{1/2}Na_{1/2})TiO_3$-$BaTiO_3$ Piezoelectrics, Phys. Rev. Lett. **109**, 107602 (2012).

[11] A. M. Glazer, The classification of tilted octahedra in perovskites, Acta Crystallogr., Sect. B: Struct. Crystallogr. Cryst. Chem. **28**, 3384 (1972).

[12] W. Setyawan and S. Curtarolo, High-throughput electronic band structure calculations: Challenges and tools, Comput. Mater. Sci. **49**, 299 (2010).

[13] M. Acosta, L. A. Schmitt, C. Cazorla, A. Studer, A. Zintler, J. Glaum, H. J. Kleebe, W. Donner, M. Hoffman, J. Rodel, and M. Hinterstein, Piezoelectricity and rotostriction through polar and non-polar coupled instabilities in bismuth-based piezoceramics, Sci. Rep. **6**, 28742 (2016).

[14] J. J. Yao, N. Monsegue, M. Murayama, W. N. Leng, W. T. Reynolds, Q. H. Zhang, H. S. Luo, J. F. Li, W. W. Ge, and D. Viehland, Role of coexisting tetragonal regions in the rhombohedral phase of $Na_{0.5}Bi_{0.5}TiO_3$-$x$at.%$BaTiO_3$ crystals on enhanced piezoelectric properties on approaching the morphotropic phase boundary, Appl. Phys. Lett. **100**, 012901 (2012).

[15] S. E. Park and T. R. Shrout, Ultrahigh strain and piezoelectric behavior in relaxor based ferroelectric single crystals, J. Appl. Phys. **82**, 1804 (1997).

[16] L. E. Cross, Relaxorferroelectrics: An overview, Ferroelectrics **151**, 305 (1994).

[17] Y. P. Guo, H. S. Luo, D. Ling, H. Q. Xu, T. H. He, and Z. W. Yin, The phase transition sequence and the location of the morphotropic phase boundary region in $(1-x)[Pb(Mg_{1/3}Nb_{2/3})O_3]$-$xPbTiO_3$ single crystal, J. Phys.: Condens. Matter **15**, L77 (2003).

[18] D. D. Viehland and E. K. H. Salje, Domain boundary-dominated systems: Adaptive structures and functional twin boundaries, Adv. Phys. **63**, 267 (2014).

[19] W. Ge, C. Luo, Q. Zhang, C. P. Devreugd, Y. Ren, J. Li, H. Luo, and D. Viehland, Ultrahigh electromechanical response in $(1-x)(Na_{0.5}Bi_{0.5})TiO_3$-$xBaTiO_3$ single-crystals via polarization extension, J. Appl. Phys. **111**, 093508 (2012).

[20] Q. H. Zhang, X. Y. Zhao, R. B. Sun, and H. S. Luo, Crystal growth and electric properties of lead-free NBT-BT

at compositions near the morphotropic phase boundary, Phys. Status Solidi A **208**, 1012 (2011).

[21] A. N. Soukhojak, H. Wang, G. W. Farrey, and Y. M. Chiang, Superlattice in single crystal barium-doped sodium bismuth titanate, J. Phys. Chem. Solids **61**, 301 (2000).

[22] J. Yao, L. Yan, W. Ge, L. Luo, J. Li, D. Viehland, Q. Zhang, and H. Luo, Evolution of domain structures in $Na_{1/2}Bi_{1/2}TiO_3$ single crystals with $BaTiO_3$, Phys. Rev. B **83**, 054107 (2011).

[23] H. W. Zhang, G. C. Deng, A. J. Studer, X. B. Li, X. Y. Zhao, and H. S. Luo, Neutron diffuse scattering of $(1-x)(Na_{0.5}Bi_{0.5})TiO_3$-$xBaTiO_3$ relaxor ferroelectric single crystals, Scr. Mater. **86**, 5 (2014).

[24] P. M. Gehring, Neutron diffuse scattering in lead-based relaxor ferroelectrics and its relationship to the ultra-high piezoelectricity, J. Adv. Dielectr. **02**, 1241005 (2012).

[25] G. Y. Xu, G. Shirane, J. R. D. Copley, and P. M. Gehring, Neutron elastic diffuse scattering study of $Pb(Mg_{1/3}Nb_{2/3})O_3$, Phys. Rev. B **69**, 064112 (2004).

[26] G. C. Deng, S. Danilkin, H. W. Zhang, P. Imperia, X. B. Li, X. Y. Zhao, and H.S. Luo, Dynamical mechanism of phase transitions in A-site ferroelectric relaxor $(Na_{1/2}Bi_{1/2})TiO_3$, Phys. Rev. B **90**, 134104 (2014).

[27] S. B. Vakhrushev, B. E. Kvyatkovskii, N. M. Okuneva, E. L. Plachenova, and P. P. Syrnikov, Phase-transitions in sodium bismuth titanate, JETP Lett. **35**, 134 (1982).

[28] S. M. Shapiro, I. A. Zaliznyak, L. Passell, V. J. Ghosh, W. J. Leonhardt, and M. E. Hagen, HYSPEC: A crystal time-of-flight hybrid spectrometer for the spallation neutron source with polarization capabilities, Physica B: Condensed Matter **385–86**, 1107 (2006).

[29] B. Winn, U. Filges, V. O. Garlea, M. Graves-Brook, M. Hagen, C. Y. Jiang, M. Kenzelmann, L. Passell, S. M. Shapiro, X. Tong, and I. Zaliznyak, Recent progress on HYSPEC, and its polarization analysis capabilities, in *Qens/Wins 2014 - 11th International Conference on Quasielastic Neutron Scattering and 6th International Workshop on Inelastic Neutron Spectrometers*, edited by B. Frick *et al.* (EDP Sciences, Cedex A, France, 2015), Vol. 83, p. 03017.

[30] R. A. Cowley, Lattice Dynamics + Phase Transitions of Strontium Titanate, Phys. Rev. **134**, A981 (1964).

[31] W. W. Ge, C. T. Luo, C. P. Devreugd, Q. H. Zhang, Y. Ren, J. F. Li, H. S. Luo, and D. Viehland, Direct evidence of correlations between relaxor behavior and polar nano-regions in relaxor ferroelectrics: A case study of lead-free piezoelectrics $Na_{0.5}Bi_{0.5}TiO_3$-x %$BaTiO_3$, Appl. Phys. Lett. **103**, 241914 (2013).

[32] C. T. Luo, Y. J. Wang, W. W. Ge, J. F. Li, D. Viehland, O. Delaire, X. B. Li, and H. S. Luo, Hierarchical domain structure of lead-free piezoelectric $(Na_{1/2}Bi_{1/2})TiO_3$-$(K_{1/2}Bi_{1/2})TiO_3$ single crystals, J. Appl. Phys. **119**, 174102 (2016).

[33] Y. Kitanaka, M. Ogino, K. Hirano, Y. Noguchi, M. Miyayama, Y. Kagawa, C. Moriyoshi, Y. Kuroiwa, S. Torii, and T. Kamiyama, Crystal structural analyses of ferrielectric tetragonal $(Bi_{1/2}Na_{1/2})TiO_3$-7%$BaTiO_3$ powders and single crystals, Jpn. J. Appl. Phys. **52**, 09KD01 (2013).

[34] ©2015 by Fachinformationszentrum Karlsruhe, ICSD code: 189275: https://www.fiz-karlsruhe.de/icsd.html.

[35] P. M. Gehring, S. Wakimoto, Z. G. Ye, and G. Shirane, Soft Mode Dynamics Above and Below the Burns Temperature in the Relaxor $Pb(Mg_{1/3}Nb_{2/3})O_3$, Phys. Rev. Lett. **87**, 277601 (2001).

[36] I. P. Swainson, C. Stock, P. M. Gehring, G. Y. Xu, K. Hirota, Y. Qiu, H. Luo, X. Zhao, J. F. Li, and D. Viehland, Soft phonon columns on the edge of the Brillouin zone in the relaxor $PbMg_{1/3}Nb_{2/3}O_3$, Phys. Rev. B **79**, 224301 (2009).

[37] P. Ondrejkovic, J. Hlinka, M. Kempa, J. Kulda, H. Luo, and Q. Zhang, Inelastic neutron scattering study of lead-free relaxor ferroelectric $(Na_{0.5}Bi_{0.5})_{0.96}Ba_{0.04}TiO_3$ single crystal, Phase Transitions **84**, 829 (2011).

[38] C. Stock, D. Ellis, I. P. Swainson, G. Y. Xu, H. Hiraka, Z. Zhong, H. Luo, X. Zhao, D. Viehland, R. J. Birgeneau, and G. Shirane, Damped soft phonons and diffuse scattering in 40%$Pb(Mg_{1/3}Nb_{2/3})O_3$-60%$PbTiO_3$, Phys. Rev. B **73**, 064107 (2006).

[39] J. J. Yao, Y. D. Yang, N. Monsegue, Y. X. Li, J. F. Li, Q. H. Zhang, W. W. Ge, H. S. Luo, and D. Viehland, Effect of Mn substituents on the domain and local structures of $Na_{1/2}Bi_{1/2}TiO_3$-$BaTiO_3$ single crystals near a morphotropic phase boundary, Appl. Phys. Lett. **98**, 132903 (2011).

[40] W. W. Ge, C. T. Luo, Q. H. Zhang, Y. Ren, J. F. Li, H. S. Luo, and D. Viehland, Evolution of structure in $Na_{0.5}Bi_{0.5}TiO_3$ single crystals with $BaTiO_3$, Appl. Phys. Lett. **105**, 162913 (2014).

[41] H. Fu and R. E. Cohen, Polarization rotation mechanism for ultrahigh electromechanical response in single-crystal piezoelectrics, Nature (London) **403**, 281 (2000).